Applied Surface Science 693 (2025) 162750

Contents lists available at ScienceDirect

Applied Surface Science

journal homepage: www.elsevier.com/locate/apsusc

Full Length Article

Enhancing selectivity and sensitivity in gas sensors through noble metal-decorated ZnO and machine learning

Yeong Min Kwon [a], Yeseul Son [b], Do Hyung Lee [a], Min Hyeok Lim [a], Jin Kyu Han [c], Moonjeong Jang [d], Seoungwoong Park [a], Saewon Kang [a], Soonmin Yim [a], Sung Myung [a], Jongsun Lim [a], Sun Sook Lee [a], Garam Bae [e,*], Soo-Hyun Kim [b,*], Wooseok Song [a,f,**]

[a] Thin Film Materials Research Center, Korea Research Institute of Chemical Technology (KRICT), 141 Gajeong-ro, Yuseong-gu, Daejeon 34114, Republic of Korea
[b] School of Materials Science and Engineering, Ulsan National Institute of Science and Technology (UNIST), Ulsan 44919, Republic of Korea
[c] Institute of Materials Research and Engineering, A*STAR (Agency for Science, Technology and Research), 138634 Singapore, Singapore
[d] National Nano Fab Center (NNFC), Daejeon 34141, Republic of Korea
[e] Department of Physics, Dankook University, Cheonan 31116, Republic of Korea
[f] Department of Electrical and Computer Engineering, Sungkyunkwan University, Suwon 16419, Republic of Korea

ARTICLE INFO

Keywords:
Next-generation gas sensors
Functionalization
Sensor array
Pattern recognition algorithm

ABSTRACT

The growing need for highly sensitive and selective gas sensors has spurred extensive research on enhancing metal–oxide–semiconductor-based sensors. In this study, we explored the gas-sensing performance of ZnO thin films functionalized with noble metals (Ir, Ru, and IrRu alloys) via atomic layer deposition for the detection of hazardous gases. The incorporation of noble metals led to significant improvements in the gas-sensing behavior driven by both electronic and chemical sensitization mechanisms. To further enhance gas selectivity, machine learning-based data analysis was employed, enabling precise classification of various gases with 100 % accuracy. These findings underscore the potential of noble metal-functionalized ZnO sensors for advanced gas detection, illustrating the effective combination of material engineering and cutting-edge data analysis techniques for the development of intelligent, selective, and stable gas sensor platforms.

1. Introduction

The widespread emission of hazardous gases, including propane (C_3H_8), carbon monoxide (CO), hydrochloric acid (HCl), ammonia (NH_3), sulfur dioxide (SO_2), and volatile organic compounds (VOCs) such as acetone, ethanol, and benzene, primarily resulting from human activities like transportation, industrial production, landfill operations, and livestock farming, has escalated concerns over public health, environmental degradation, and the intensification of global warming across both urban and rural areas [1–6]. Consequently, researchers are actively innovating and developing advanced gas sensors for the precise and efficient detection and monitoring of hazardous gases that threaten both environmental safety and human health. Among the diverse range of gas sensors, metal–oxide–semiconductor (MOS)-based sensors have garnered significant attention owing to their numerous advantages, including high sensitivity, compactness, ease of fabrication, straightforward operation, and cost-effective production [7,8].

However, MOS-based sensors have a significant drawback in terms of their low selectivity because they typically respond to a wide variety of gases. To address this limitation, pioneering researchers have often focused on surface functionalization or incorporation of additives into metal oxides to modulate their intrinsic electronic properties, thereby enhancing their selective sensing capabilities. Extensive research has focused on improving the selectivity of gas sensors by introducing heteromaterials, including non-metals such as graphene, graphene quantum dots, CNTs, *h*-BN, and *g*-C_3N_4 [9–13], metals such as Au, Pt, Pd, Ni, and Cu [14–18], and transition metal chalcogenides, including ZnS, $MoSe_2$, MoS_2, CdS, and WSe_2 [19–23], in combination with metal oxides such as ZnO, SnO_2, TiO_2, and CuO [24–27]. Despite these advancements, single sensors often face difficulties in accurately identifying a vast array of hazardous gases in industrial environments. Therefore, achieving high-performance, cost-effective, accurate, and stable air monitoring

* Corresponding authors.
** Corresponding author at: Thin Film Materials Research Center, Korea Research Institute of Chemical Technology (KRICT), 141 Gajeong-ro, Yuseong-gu, Daejeon 34114, Republic of Korea.
E-mail addresses: grbae@dankook.ac.kr (G. Bae), soohyunsq@unist.ac.kr (S.-H. Kim), wssong@krict.re.kr (W. Song).

https://doi.org/10.1016/j.apsusc.2025.162750
Received 2 January 2025; Received in revised form 7 February 2025; Accepted 20 February 2025
Available online 21 February 2025

requires not only the enhancement of sensor capabilities through functionalized sensing materials but also the integration of multiple MOS sensor arrays combined with advanced data processing technologies [28–30].

In this study, we demonstrated MOS gas-sensor arrays utilizing ZnO and functionalized ZnO thin films (Ir, Ru, and IrRu-ZnO). These gas-sensor arrays exhibited exceptional stability, reliability, and gas-sensing performance. Moreover, because both the ZnO and metal decoration processes utilize atomic layer deposition (ALD), this approach offers significant advantages for seamless production continuity. To enhance selective gas identification capability, we developed an machine learning (ML) classification model based on a statistical data process for identifying various gas species. This approach achieves outstanding prediction accuracy and clarity by utilizing pre-manipulated feature data. Our strategy demonstrates the potential for ML-based classification, offering superior visibility for the development of highly sensitive and selective gas sensor platforms.

2. Materials and methods

2.1. Synthesis of sensing materials

2.1.1. Pristine ZnO thin film

Gas sensors based on pristine and metal-decorated ZnO thin films were fabricated *via* ALD [31]. First, pristine ZnO thin films were deposited by ALD onto clean SiO_2/ Si substrates by introducing diethylzinc (DEZ, Sigma-Aldrich) and deionized water (18.2 MΩ, Milli-Q) as the Zn and O sources, respectively. The substrate and DEZ source were set to room temperature. Ar (99.999 %, Jung-Ang Gas tech.) was used as the purge gas. The optimal ZnO thin film ALD was implemented in the following sequence: DEZ supply (0.4 s), Ar purge (10 s), deionized water supply (1 s), and Ar purge (10 s). The thickness of the ZnO thin films can be modulated by repeating the ALD cycles, which is a representative advantage for the implementation of laminated nanofilms with high uniformity and reliability over a large area. The optimal ZnO thickness was determined as 30 nm by repeating 159 cycles at a deposition rate of 0.188 nm/cycle.

2.1.2. Heteroatomic hybridization with noble metal nanoparticles

Ir thin films were deposited in a traveling-wave-type ALD reactor (NCD Technology, Lucida D100, Korea) using a tricarbonyl (1,2,3-η)-1,2,3-tri(*tert*-butyl)-cyclopro-penyl iridium ($C_{18}H_{27}IrO_3$ or TICP) precursor and O_2 (99.999 %). TICP was synthesized by TANAKA Precious Metals (Japan) using a previously reported process.[32]. The range of deposition temperature was 250°C. The standard cycle of Ir ALD consisted of precursor pulsing for 7 s, reactant pulsing for 5 s, and purging for 10 s. This process was established based on the self-limiting growth criteria discussed below. The precursor was heated at 55 °C to obtain a suitable vapor pressure during film deposition. N_2 (100 sccm) was used as the carrier and purge gas for the metal precursor and was also used between two consecutive pulses during deposition.

Ru-ALD was performed using the same traveling-wave-type ALD reactor (NCD Technology, Lucida D100, Korea) with [Ru(TMM)$(CO)_3$] (TANAKA Precious Metals, Japan) and O_2 as the precursor and reactant, respectively [33]. [Ru(TMM)$(CO)_3$] was stored in a stainless-steel canister, which was maintained at 10 °C using a cooling system. The Ru precursor was pulsed into the chamber by N_2 gas at a flow rate of 50 sccm. The gas flow rates of reactant O_2 and purged N_2 were 50 and 100 sccm, respectively. The deposition temperature was 220 °C. One cycle of Ru ALD was composed of a 10 s [Ru(TMM)$(CO)_3$] pulse, 10 s N_2 purge, 10 s O_2 pulse, and 10 s N_2 purge. The GPC of the Ru ALD was ≈ 1.7 Å cycle^{-1}.

IrRu alloy- films were deposited by repeating the super-cycles consisting of Ir and Ru ALD sub-cycles at a deposition temperature of 250 °C and a working pressure of approximately 0.5 Torr using the same traveling-wave-type ALD reactor (NCD Technology, Lucida D100, Korea). Each sub-cycle consisted of several unit cycles. A single-unit cycle comprised a precursor injection pulse, purge pulse, reactant injection pulse, and purge pulse. TICP and [Ru(TMM)$(CO)_3$] were used as the Ir and Ru precursors, respectively, and were carried to the chamber using N_2 gas. The gas flow rates of reactant O_2 and purged N_2 were 50 and 100 sccm, respectively. The Ir-ALD cycle consisted of precursor pulsing for 7 s, reactant pulsing for 5 s, and purging for 10 s. One cycle of Ru ALD was composed of a 10 s [Ru(TMM)$(CO)_3$] pulse, 10 s N_2 purge, 10 s O_2 pulse, and 10 s N_2 purge. By combining these two processes, ALD Ir-Ru films could be deposited. Here, the number of Ir subcycles was fixed at 30, and the number of overall supercycles consisting of Ir and Ru subcycles was 2. The final ALD-Ir step was performed to prevent oxidation of the Ru film by air exposure after deposition. In each supercycle, the number of Ru ALD sub-cycles was fixed at seven immediately after the Ir sub-cycles to prepare ALD Ir-Ru films with various compositions.

2.2. Material characterization

The chemical characteristics of ZnO and the novel metal (Ir, Ru, and IrRu alloy)-coated ZnO films were investigated by X-ray photoelectron spectroscopy (XPS, K-Alpha, Thermo Fisher Scientific). The surface morphologies and thicknesses of the ZnO and novel metal-coated ZnO thin films were characterized using atomic force microscopy (AFM, Innova, Bruker) and field-emission scanning electron microscopy (FE-SEM, JSM-6700F, Jeol). The gas sensing measurements were conducted by a customized gas characterization system (≈1111 cm^3, MSTECH) integrated with a gas flow controller (SR312, Bronkhorst High-tech) and an electric source meter (Keithley 2612B, Keithley). To measure the electrical characteristics of the ZnO thin films, a bias sweep from −3 to 3 V was applied across the electrodes at 250 °C under ambient pressure. All the gas sensing measurements were performed at 250 °C under ambient pressure with an applied bias of 1 V.

2.3. Data preparation for machine learning

To collect feature data and answer datasets for machine learning, we applied a customized exponential curve-fitting algorithm using a standard open library in Python for the recorded dynamic gas response curves of the surface-engineered ZnO-based sensors. For the feature data, four extracted parameters, including exponential fitting constants and integration under the signal curve, were obtained for a single curve. Regarding the four different sensor devices and two different signal curves (response and recovery), we established our feature dataset with 32 characteristic parameters (four features × two regions × four sensors) for a single gas measurement, and the corresponding gas types were allocated as the answer dataset. The classification was evaluated using standard training algorithms, including logistic regression, decision tree, random forest, k-nearest neighbor (kNN), Naïve Bayes, support vector machine (SVM), XGBoost, light gradient boosting machine (GBM), CatBoost, and neural network models with the k-fold validation method (k = 5) using Python machine learning libraries. The trained model was evaluated based on the accuracy, precision, recall, and F1 scores. The correlations between the features and predictions were analyzed using the mean SHAP value.

3. Results and discussions

The surface engineering of chemoresistive metal oxide materials is an efficient and facile method that is widely used in various aspects of gas sensor arrays. By varying the functionalization of the oxide surface, the device performance can be purposefully modulated, and the interactions with gas analytes can be improved. Typically, metal oxide gas sensor surfaces are modified with noble metals, especially those from the platinum group (Pt, Pd, Ir, Ru, and Rh), to induce spillover or electron sensitization effects, thereby significantly enhancing the sensing

performance. Fig. 1(a) shows schematic images of the ZnO nanofilms prepared using ALD. As mentioned above, the optimal thickness of ZnO was rationally determined to be 30 nm by repeating 159 cycles at a deposition rate of 0.188 nm/cycle. Following the deposition of the ZnO thin films, we implemented surface customization using ALD of Ir, Ru, and IrRu alloys. To evaluate the surface morphologies of the metal (Ir, Ru, and IrRu alloy)–ZnO hybrid thin films, we conducted FE-SEM analysis for pristine ZnO and 3 nm-thick Ir, Ru, and IrRu alloy–ZnO nanofilms, as shown in Fig. 1(b–e) and S1, respectively. The cross-sectional FE-SEM images of the pristine ZnO thin film confirm that the film thickness is approximately 30 nm, consistent with our ALD cycle design. SEM observations revealed that the ZnO nanofilms exhibited round-grained structures, and the ZnO films coated with Ir, Ru, and IrRu alloys were conformally decorated on the ZnO surfaces. After coating the metals onto ZnO, the change in the morphology appeared to be negligible, as shown in the SEM images. To complement the SEM morphological analysis, we performed atomic force microscopy (AFM) topographical observations of pristine ZnO, Ir-ZnO, Ru-ZnO, and IrRu-alloy-ZnO, as represented in Fig. 1(f-i). The root-mean-square (RMS) roughness values of pristine ZnO, Ir-ZnO, Ru-ZnO, and IrRu alloy-ZnO were 1.07, 1.09, 0.99, and 1.00, respectively, indicating that a highly conformal coated surface was achieved through the ALD process.

To explore the evolution of the chemical states of ZnO thin films coated with metals (Ir, Ru, and IrRu alloys), we conducted comprehensive X-ray photoemission spectroscopy (XPS) analyses. The survey spectrum of the pristine ZnO nanofilms reveals the presence of Zn and O, as shown in Fig. 2(a). Following the incorporation of Ir, Ru, and IrRu into the ZnO nanofilms, the chemical states corresponding to Ir and Ru became evident in the survey spectra, as shown in Fig. 2(e, j, o). The Zn 2*p* core level spectra exhibit two distinct doublet peaks corresponding to the Zn $2p_{3/2}$ and Zn $2p_{1/2}$ bonding states, located at binding energies (E_B) of 1021.7 eV and 1044.8 eV, respectively. These peaks indicate the formation of stoichiometric ZnO regardless of the type of metal coating, as shown in Fig. 2(b, f, k, p). Fig. 2(c, g, l, q) displays the O 1*s* core-level spectra for both pristine and metal-decorated ZnO nanofilms. The deconvoluted O 1*s* core-level spectrum, as shown in figure S2, comprises three distinguishable components: loosely bound oxygen on the ZnO surface (E_B = 533.4 eV), O^{2-} ions near oxygen vacancies (E_B = 531.88 eV), and O^{2-} ions coordinated with Zn atoms in the hexagonal wurtzite structure (E_B = 530.18 eV) [34,35]. This spectrum indicates that the surface-adsorbed oxygen on IrRu alloy-coated ZnO is relatively lower compared to that on single-metal decorated ZnO (Ir- and Ru-ZnO). These findings indicated that there was no significant shift in the binding energy or notable alteration in the spectral shape of the Zn 2*p* and O 1*s* core-level spectra after metal hybridization. After the deposition of the nanometric metal layers onto the ZnO nanofilms, a noticeable reduction in the intensities of the two peaks was observed, likely owing to the suppression of the ZnO vibrational modes induced by the metal coatings. Furthermore, Fig. 2(d) presents a photographic image of both pristine and metal-decorated ZnO nanofilms, confirming that there was negligible damage to the sensor devices during the high-temperature metal deposition process. Fig. 2(h, m, r) show the Ir 4*f* core-level spectra of the pristine and metal-decorated ZnO nanofilms. The Ir 4*f* spectra exhibit two distinct peaks corresponding to the Ir $4f_{7/2}$ and $4f_{5/2}$ doublet at binding energies of 60.9 eV and 63.9 eV, respectively, indicating the formation of metallic Ir^0. In addition, the C 1*s* and Ru 3*d* peaks are discernible in the same binding energy region, as shown in Fig. 2(i, n, s). The Ru 3*d* core level spectra also reveal two pronounced peaks attributed to the Ru $3d_{5/2}$ and $3d_{3/2}$ bonding states at binding energies of 280.1 eV and 284.3 eV, respectively, indicating the formation of

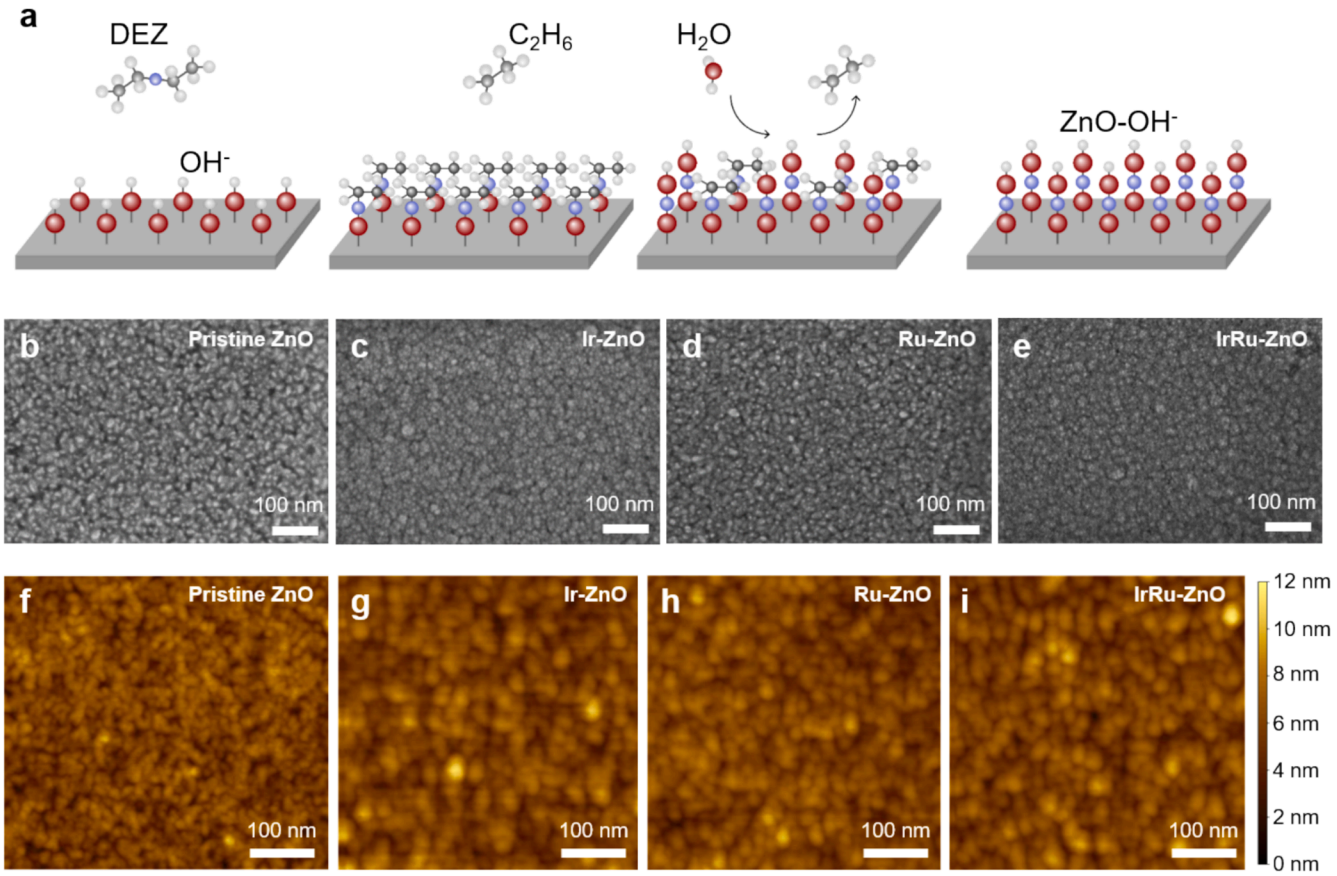

Fig. 1. (a) Schematic images of atomic layer deposition (ALD) process for ZnO nanofilm. Scanning electron microscopy (SEM) images of synthesized (b) pristine ZnO, (c) Ir-, (d) Ru-, and (e) IrRu alloy-coated ZnO nanofilm. Atomic force microscopy (AFM) images of (f) pristine ZnO, (g) Ir-, (h) Ru-, and (i) IrRu alloy-coated ZnO nanofilm.

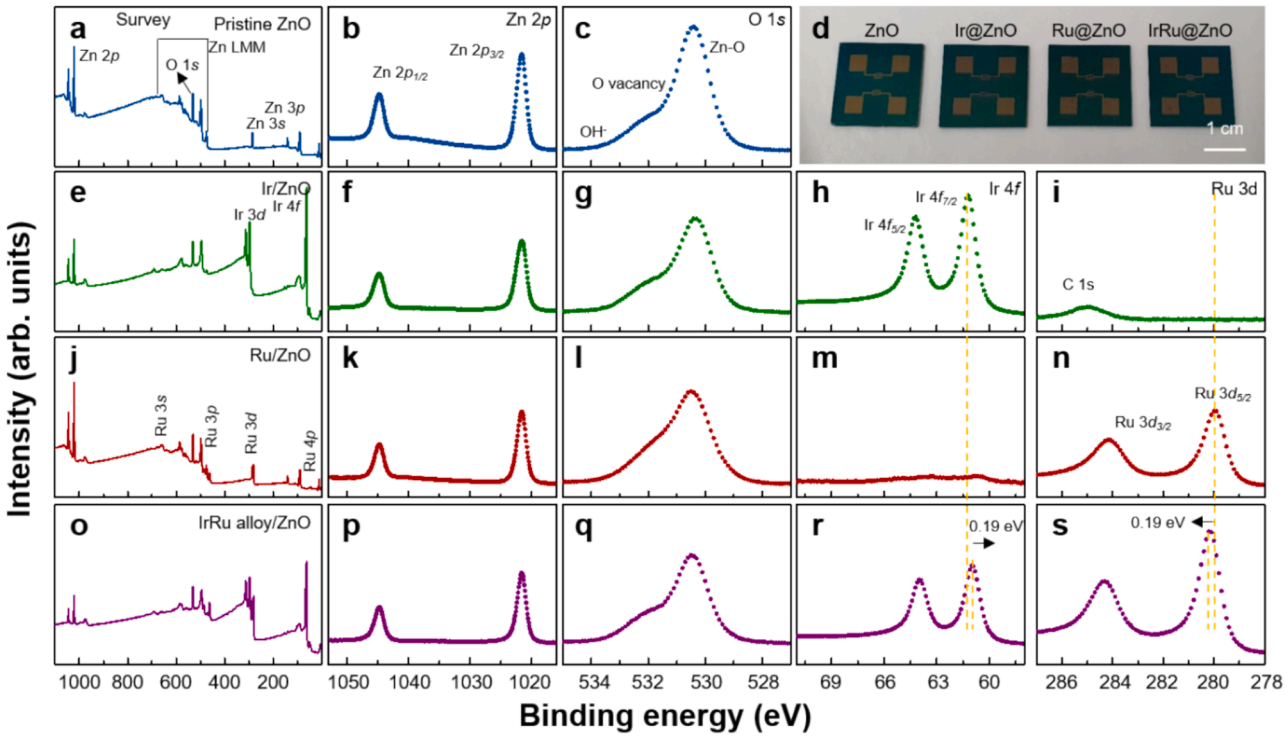

Fig. 2. Chemical identification of pristine ZnO and metal-decorated ZnO nanofilms using X-ray photoelectron spectroscopy (XPS). XPS spectra of pristine ZnO: (a) survey, (b) Zn 2*p*, and (c) O 1*s*. (d) Photographic image of pristine ZnO and metal decorated ZnO nanofilms. XPS spectra of Ir-ZnO, Ru-ZnO, and IrRu alloy ZnO: (e) survey, (f) Zn 2*p*, (g) O 1*s*, (h) Ir 4*f*, and (i) Ru 3*d* core levels from Ir-ZnO. (j) survey, (k) Zn 2*p*, (l) O 1*s*, (m) Ir 4*f*, and (n) Ru 3*d* core levels from Ru-ZnO. (o) Survey, (p) Zn 2*p*, (q) O 1*s*, (r) Ir 4*f*, and (s) Ru 3*d* core levels from IrRu alloy-ZnO.

metallic Ru^0 [36].

The deposition of the IrRu alloy was confirmed by the discernible presence of both Ir and Ru core-level spectra, as shown in Fig. 2(r, s), verifying the successful incorporation of the IrRu metal alloy. Notably, the Ir 4*f* core level of the IrRu alloy shifted toward a lower binding energy compared to that of pristine Ir. In contrast, Ru 3*d* shifted toward a higher binding energy compared to pristine Ru. These shifts suggest that the electronic states of Ir and Ru are modulated by alloy formation [36,37]. This indicates that the deposition of the metal nanofilms did not significantly alter the intrinsic structural or chemical properties of ZnO, which remains the primary active sensing material. Thus, secondary effects such as those arising from chemical functionalization, electronic structure engineering, or charge transfer mechanisms can be reasonably excluded from influencing the principal sensing behavior [34].

Two-terminal gas sensors were fabricated using a shadow mask to assess the gas-sensing performance of the hybrid material-based sensors. To investigate the influence of different gases and deposited catalytic metals on the material reactivity, gas response measurements were conducted on pristine ZnO and ZnO coated with Ir, Ru, and IrRu alloys under various gas types and concentrations. Before measuring the gas responses of each sensor, we established the baseline resistance of the devices by measuring the I-V curves at 250 °C, as shown in Fig. S3 and Table S1. From these results, we demonstrate that the surface modification is likely attributable to regulating the spill-over effect. Dry air was rationally selected as the base gas, and the total gas flow rate was maintained at 1000 sccm for all experiments. The dynamic gas response curves of the ZnO-, Ir@ZnO-, Ru@ZnO-, and IrRu@ZnO-based sensors at 250 °C for 8 different gases—acetone (20–80 ppm), benzene (4–16 ppm), ethanol (20–80 ppm), HCl (4–16 ppm), CO (20–80 ppm), NH_3 (20–80 ppm), propane (0.2–0.8 %), and SO_2 (4–16 ppm) are presented in Fig. 3(a-h). The gas response was determined by calculating the percentage change in sensor resistance, defined by the equation: gas response (%) $= (R_{gas} - R_0)/R_0 \times 100$, where R_{gas} represents the resistance under exposure to the target gas, and R_0 refers to the resistance in the baseline state. The gas-sensing mechanism of ZnO-based sensors is governed by a typical metal oxide semiconductor oxygen adsorption model [38]. At temperatures above 150 °C, oxygen molecules from the air adsorb onto the ZnO surface, capturing electrons from ZnO and forming chemisorbed oxygen species (O_2^-, O^-, or O^{2-}), which leads to the creation of an electron depletion layer, thereby increasing the resistance of ZnO [39]. The relevant reaction processes are as follows:

$$O_2\,(gas) \rightarrow O_2\,(ads) \quad (1)$$

$$O_2\,(ads) + e^- \rightarrow O_2^-\,(ads) \quad (2)$$

$$O_2^-(ads) + e^- \rightarrow 2O^-\,(ads) \quad (3)$$

$$O^-\,(ads) + e^- \rightarrow O^{2-}\,(ads) \quad (4)$$

When ZnO is exposed to target gases, the gas molecules that are adsorbed interact with the chemisorbed oxygen species. This interaction can either lead to the release of electrons back to ZnO in the case of reducing gases, or cause the withdrawal of more electrons from ZnO in the case of oxidizing gases, depending on the redox properties of the gases. This process altered the width of the electron depletion layer, leading to a corresponding change in the resistance of ZnO. Specifically, when a reducing gas is introduced, the electron depletion layer narrows, resulting in a decrease in the resistance of ZnO. Conversely, exposure to an oxidizing gas causes expansion of the depletion layer, thereby increasing the resistance of ZnO. This change in resistance was directly correlated with the response of the gas sensor.

It is well-recognized that noble metals exhibit catalytic effects that significantly enhance the gas-sensing performance of metal oxide sensors. The improvement in gas sensing after noble metal decoration is primarily attributed to two mechanisms: electronic and chemical sensitization. In electronic sensitization, the majority of carriers are transferred from noble metals to ZnO owing to a work function mismatch, resulting in the formation of potential barriers. Because the

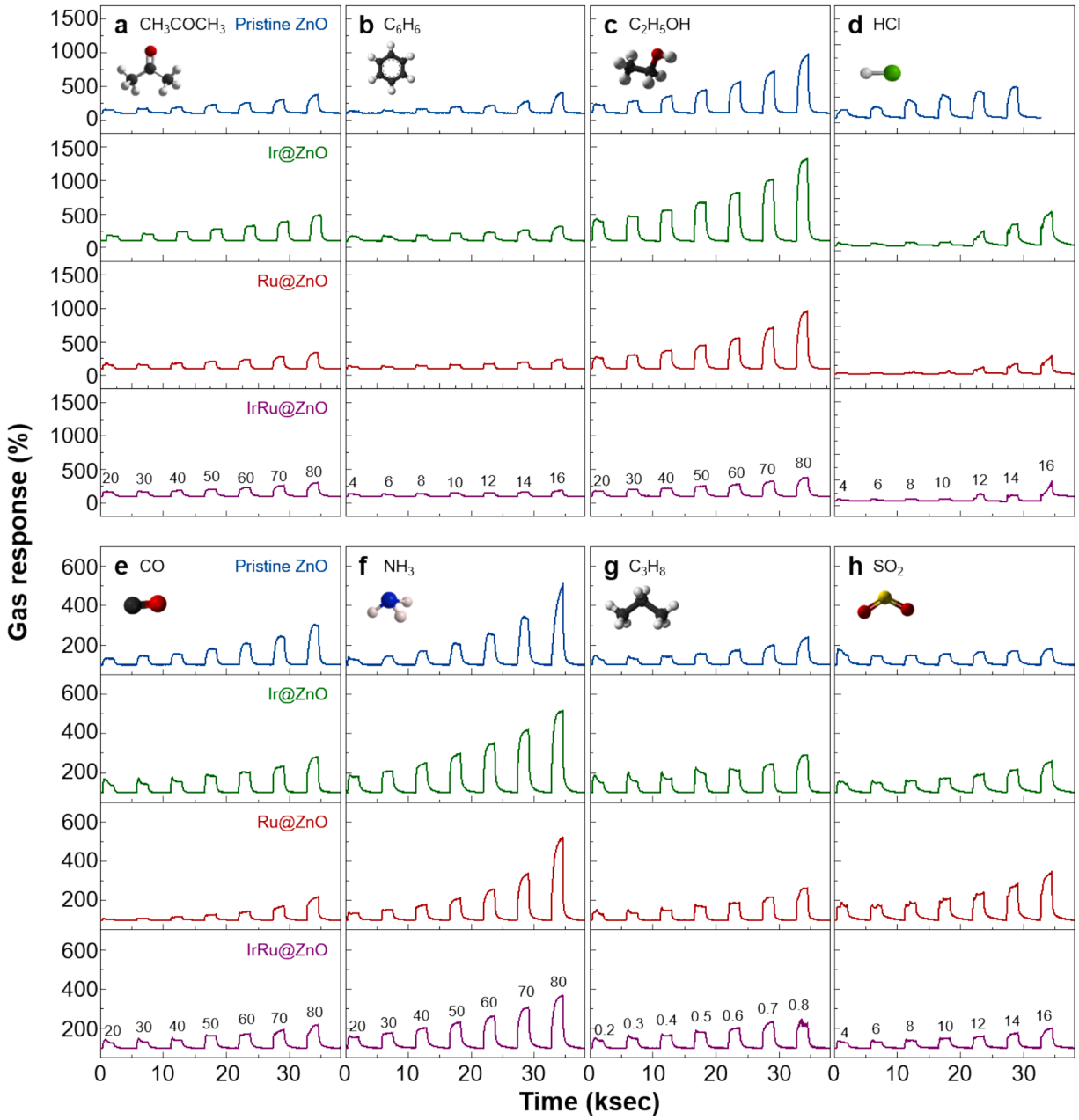

Fig. 3. Gas sensing performances of pristine ZnO, Ir-, Ru-, and IrRu alloy-ZnO nanofilms-based gas sensors for (a) CH_3COCH_3, (b) C_6H_6, (c) C_2H_5OH, (d) HCl, (e) CO, (f) NH_3, (g) C_3H_8, and (h) SO_2 gases.

work function of noble metals is higher than that of ZnO, the electrons generated during the sensing process flow from the conduction band of ZnO to the noble metals until the Fermi levels equalize [40–42]. This leads to the formation of a Schottky barrier and an increase in the thickness of the electron-depletion layer. These effects prevent the recombination of electron-hole pairs, resulting in significant resistance changes when exposed to target gases, thereby amplifying the sensor's response.

Chemical sensitization, also known as the spillover effect, occurs when noble metals facilitate the dissociation of oxygen molecules into reactive chemisorbed oxygen ions, which then "spill over" to the ZnO surface and react with gas molecules [43,44]. Oxygen molecules preferentially adsorb onto the surface of noble metal nanoparticles, dissociate into O_2^-, O^-, and O^{2-}, and then migrate to the ZnO surface. For example, in the presence of a reducing gas, the abundant O^- ions react with a larger number of gas molecules, releasing electrons and rapidly altering the sensor's resistance, significantly boosting gas sensing performance. Moreover, noble-metal nanoparticles increase the specific surface area of the sensing material, providing more catalytically active sites for gas adsorption and diffusion.

To provide a clear comparison of the gas response of ZnO based on the type of deposited metal, the response values as a function of gas concentration were extracted from the dynamic gas response curves in Fig. 3 and are presented in Fig. S4(a-h) and S5(a-e), which is further compared with previous literature as summarized Table S2. The results consistently demonstrate an increase in response to increasing gas concentrations, irrespective of the type of gas (acetone, benzene, ethanol, HCl, CO, NH_3, propane, and SO_2) or metal (Ir, Ru, and IrRu alloy) used. This behavior aligns with the oxygen adsorption model of ZnO-based gas sensors, in which higher target gas concentrations enhance reactions with surface-adsorbed oxygen species, resulting in significant changes in the resistance of the material [45]. Intriguingly,

we discovered that ZnO decorated with IrRu alloy, initially anticipated to exhibit the highest reactivity, demonstrated the lowest gas reactivity due to the following reasons. As mentioned above, the decoration of catalytic-metal nanoparticles induces a spill-over effect, which lowers the Gibbs free energy required for gaseous oxygen molecules to be adsorbed onto the metal surface, thereby facilitating chemical bonding and reducing the availability of oxygen ions for gas reactions. However, according to pioneer researches, while metal catalysts lower the adsorption energy of oxygen ions, they also reduce the energy required for the reduction from the ionized oxygen to oxygen molecules, making it imperative to carefully regulate the type and quantity of the metal catalyst [8,16]. Considering the DFT calculation results from prior research, it was observed that the IrRu alloy exhibits a high energy barrier for oxygen gas desorption [46]. Considering the DFT calculation results from prior research and the deconvoluted O1*s* core-level spectra analysis of IrRu/ZnO, it was observed that the IrRu alloy exhibits a high energy barrier for oxygen gas desorption [46]. From the Fig. S2 and S3, we demonstrate that the surface-adsorbed oxygen for IrRu alloy-coated ZnO was relatively low, compared to the single-metal decorated ZnO (Ir- and Ru-ZnO). In addition, the I-V curve of IrRu/ZnO measured at 250 °C also presented the lowest baseline resistance, which further supported the XPS analysis. Interestingly, contrary to our initial hypothesis that metal deposition would universally improve the reactivity, we found that certain gases, such as HCl, exhibited the highest reactivity with pristine ZnO. This phenomenon can be explained by the rapid oxidation reaction between ZnO and HCl, as shown in the following equation, which leads to surface etching and a sharp decline in electrical conductivity.

$$2HCl + ZnO \rightarrow ZnCl_2 + H_2O$$

As depicted in Fig. S6, the etching of the ZnO surface reveals the underlying SiO_2/Si substrate, confirming the disruption of the electrical contact of ZnO and the gas response driven by rapid oxidation. In contrast, when Ir or Ru is deposited, the Pt-group metals, which are known for their superior corrosion resistance, create a surface passivation effect that significantly reduces the etching caused by HCl exposure. To assess the stability of the metal-coated ZnO sensor, we exposed the IrRu-ZnO device to HCl gas for five months and subsequently evaluated its gas reactivity (Fig. S7). We demonstrate that IrRu decoration leads to enhanced sensing stability for ZnO-based gas sensors even after prolonged exposure. Furthermore, previous studies have indicated that the optimal gas reaction temperature can vary depending on the type and concentration of the deposited metal. This implies that at a fixed temperature of 250 °C, the gas reactivity may decrease for specific gases, even with noble metal decoration on the surface, owing to the unique interactions between the gas molecules and the metal [47–49].

Generally, the gas response is influenced by the selectivity and concentration of the target gas. This implies that distinguishing between a low-concentration gas with a high reactivity and a high-concentration gas with a relatively low reactivity can be challenging if the response curves are similar. However, the deposition of Ir, Ru, and IrRu alloys induced both increases and decreases in gas reactivity, enhancing the ability of the gas sensor array to differentiate between various gases. Among the noble-metal-modified ZnO samples, the Ir-decorated sensor notably favored ethanol, likely because Ir effectively lowers reaction barriers for partial oxidation steps and enhances oxygen spillover on the ZnO surface. This combination accelerates the formation and removal of ethanol-derived intermediates (e.g., CH_3CHO), leading to a more pronounced and selective response for ethanol [46]. From I-V curve measurements (Fig. S3), we also confirmed that IrRu–ZnO features a relatively lower baseline resistance compared to Ir–ZnO and Ru–ZnO. Consequently, identical absolute changes in resistance (ΔR) yield smaller normalized signals ($\Delta R/R_0$), which may reduce the apparent gas response even if IrRu–analyte interactions remain strong. This differentiation can be further improved using advanced data analysis techniques, such as machine learning (ML) methods. These techniques allow for more precise gas identification by capturing subtle variations in reactivity [27–30,50].

Fig. 4(a) shows a schematic of the general process for the ML-driven classification of several gas species: acetone (CH_3COCH_3), benzene (C_6H_6), CO, ethanol (CH_3CH_2OH), HCl, NH_3, propane, and SO_2. First, we obtained the dynamic gas response and recovery curves of the surface-engineered ZnO-based sensors (pristine ZnO, Ir-ZnO, Ru-ZnO, and IrRu-ZnO) for 8 different gas species at various concentrations. The dynamic gas response curve corroborated the gas injection-dependent variation in the electrical signal. In addition, the response can further suggest several additional features, reflecting the activating dynamics of the gas molecule–sensor material interactions under gas adsorption and desorption. Since two classes of datasets consisting of labeled data (or answer data) and feature data are needed to utilize the machine learning method, we rationally assigned the class of the target gas as labeled data. For the feature data of machine learning, three parameters were extracted from the dynamic response curve via exponential curve fitting of a single curve, as represented Fig. 3a. The response curve can be regarded as a combination of two different curves in the gas response and gas recovery regions. Consequently, the individual response and recovery curves can be fitted using an exponential growth (or decay) function, as defined by

$$\text{Fitting curve} = -a_{res/rec} \cdot \exp(-k_{res/rec} \cdot t) + b_{res/rec}$$

where $a_{res/rec}$ is the initial constant, $k_{res/rec}$ is the time constant, and $b_{res/rec}$ is the offset between the response and recovery regions. In addition, we organized the feature dataset, including the integrated area under the response/recovery curves ($A_{res/rec}$) and the response values. Because we collected the gas response results from four different types of surface-engineered ZnO-based sensors, our feature dataset for the single-measured labels of the target gas species consisted of 36 features (four different sensors × nine features). To corroborate a scheme for discriminating the target gas among the 8 different groups, we employed a supervised ML approach using the extracted feature dataset. The classification was evaluated using common training algorithms, including logistic regression, decision tree, random forest, kNN, Naïve Bayes, support vector machine (SVM), XGBoost, light GBM, CatBoost, and neural network models with the k-fold validation method (k = 5). The machine learning results for classification accuracy, precision, recall, and F1 score for the various classification models are summarized in Fig. 4(b). Except for Naïve Bayes and SVM models, the classification accuracy, precision, recall, and F1 are scored 100 %. We observed high-accuracy prediction performance for most classification models, which validates the robustness and effectiveness of the proposed extraction process. The Naïve Bayes model presents 0.76, 0.77, 0.76, and 0.75 of accuracy, precision, recall, and F1 scores, respectively. The SVM were recorded as 0.43, 0.72, 0.43, and 0.50 for accuracy, precision, recall, and F1 scores, respectively. Fig. 4(c) shows the confusion matrix of 8 different target gases obtained from the classification results of the high-scoring classification models. The other confusion matrices for the Naïve Bayes and SVM models are represented in Fig. S4. Fig. 4(d) presents the mean SHAP value rankings of the covariate importance that contributed to the prediction of cluster classification using light GBM. The top five SHAP values were a_{rec4}, k_{res3}, k_{res4}, a_{res2}, and k_{rec4}, indicating that the evolution quantities in the attenuation slope of the curve contributed the most to the classification of the 8 gas species. Specifically, arec4 was clearly the most robust predictor, contributing significantly to the classification of HCL gas (SHAP = 1.20). In contrast, k_{res3} (0.79), k_{res4} (0.53), a_{res2} (0.74), k_{rec4} (0.25), A_{rec3} (0.58), k_{rec2} (0.69), and k_{rec3} (0.33), contribute to identify the CO, NH_3, ethanol, propane, SO_2, benzene, and acetone with scoring maximum SHAP value, respectively. The recorded SHAP values are presented in Table S3. From these results, we can validate that it is strongly correlated with the demonstrated ML models to our extracted feature parameters originating from the

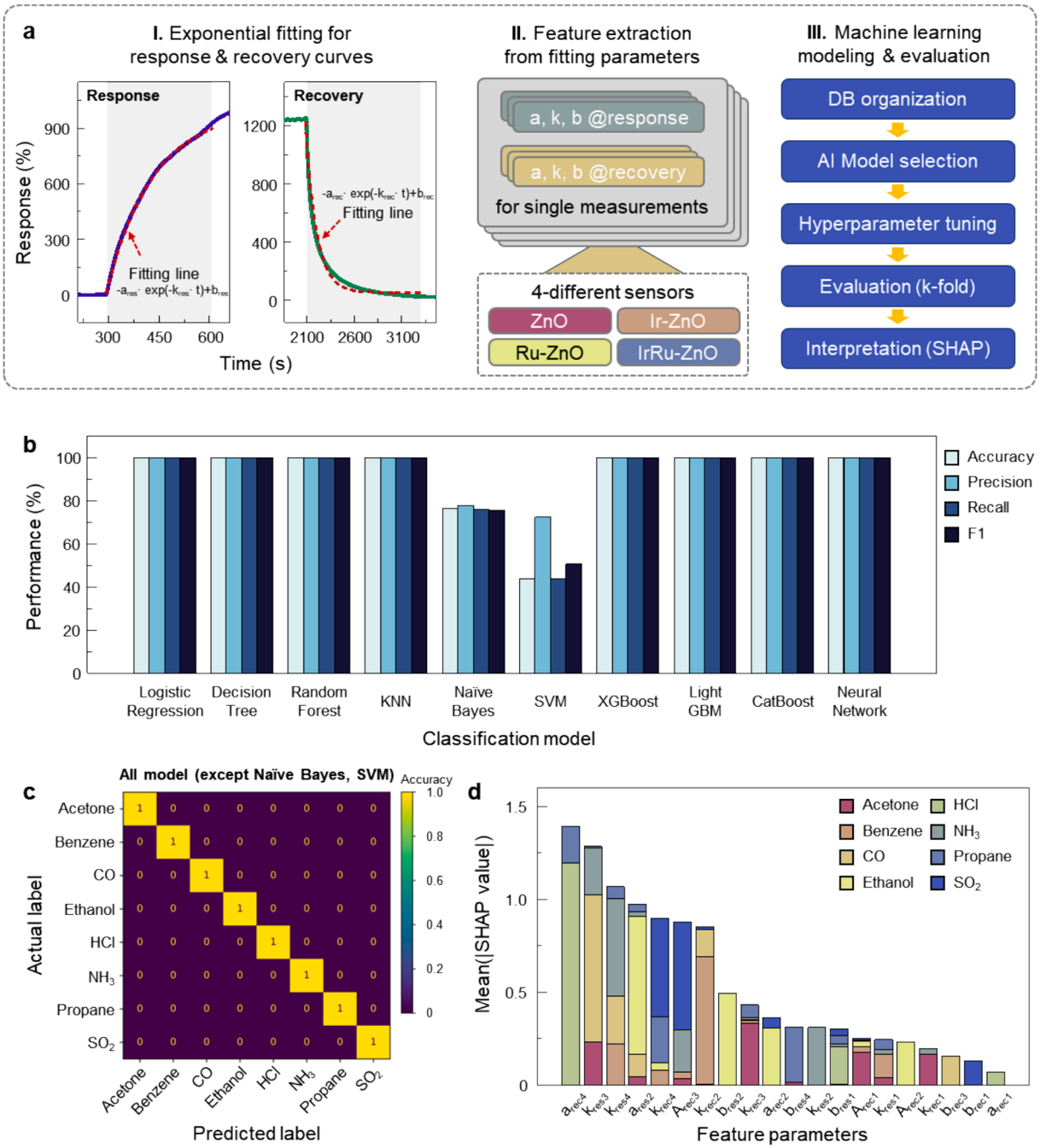

Fig. 4. (a) Schematic illustration for machine learning (ML)-driven classification, including data acquisition and feature extraction from exponential fitting parameters, ML model selection, optimization, evaluation, and interpretation. (b) ML results of prediction accuracy, precision, recall, and F1 scores for logistic regression, decision tree, random forest, kNN, Naïve Bayes, support vector machine (SVM), XGBoost, light gradient boosting machine (GBM), CatBoost, and neural network model. (c) Confusion matrix for ML-predicted results except Naïve Bayes and SVM models. (d) Mean SHAP value contribution plot of applied features for 8 different target gas species from the XGBoost model.

quantified gas dynamics with sensing materials.

4. Conclusions

In this study, we present a comprehensive evaluation of metal–oxide–semiconductor (MOS)-based gas sensors decorated with noble metals (Ir, Ru, and IrRu alloys) to enhance their gas-sensing performance. Our research demonstrates that the functionalization of ZnO with these noble metals significantly improves the gas response, which is attributed to electronic and chemical sensitization effects. Notably, the sensor arrays exhibited superior performance in detecting various hazardous gases, including acetone, benzene, HCl, and NH_3, at different concentrations. We found that the catalytic activity of noble metals plays a pivotal role in enhancing the gas reactivity, with IrRu-alloy-decorated ZnO sensors showing enhanced stability and selectivity. In addition, the implementation of machine-learning models facilitated accurate gas classification and improved sensor selectivity. The integration of functionalized materials with advanced data-processing approaches has paved the way for the development of next-generation intelligent gas sensors. Further optimization of these materials and their incorporation into multisensor arrays could significantly enhance the detection and monitoring of a wide range of hazardous gases,

contributing to improved environmental safety and industrial monitoring.

CRediT authorship contribution statement

Yeong Min Kwon: Writing – original draft, Formal analysis, Data curation. **Yeseul Son:** Formal analysis, Data curation. **Do Hyung Lee:** Investigation, Formal analysis. **Min Hyeok Lim:** Investigation, Formal analysis. **Jin Kyu Han:** Methodology, Investigation. **Moonjeong Jang:** Writing – review & editing, Formal analysis. **Seoungwoong Park:** Writing – review & editing, Investigation. **Saewon Kang:** Writing – review & editing, Formal analysis. **Soonmin Yim:** Writing – review & editing, Formal analysis, Data curation. **Sung Myung:** Writing – review & editing, Formal analysis. **Jongsun Lim:** Writing – review & editing, Methodology, Investigation. **Sun Sook Lee:** Methodology, Investigation. **Garam Bae:** Writing – original draft, Supervision, Data curation. **Soo-Hyun Kim:** Writing – review & editing, Supervision, Investigation. **Wooseok Song:** Writing – original draft, Supervision, Funding acquisition, Formal analysis, Conceptualization.

Declaration of competing interest

The authors declare that they have no known competing financial interests or personal relationships that could have appeared to influence the work reported in this paper.

Acknowledgment

This study was supported by the Nano-Material Technology Development Program through the National Research Foundation of Korea (NRF), South Korea, funded by the Ministry of Science and ICT (2021M3H4A3A02099208), South Korea. The authors also acknowledge financial support from the Development of Smart Chemical Materials for IoT Devices Project (KS2421-10) through the Korea Research Institute of Chemical Technology, South Korea.

Appendix A. Supplementary data

Supplementary data to this article can be found online at https://doi.org/10.1016/j.apsusc.2025.162750.

Data availability

The authors do not have permission to share data.

References

[1] J.P.M. Lázaro, E.S.G. López, F.L. Urias, E.M. Sandoval, O.B. Alonso, H.G. Bonilla, A. G. Bonilla, V.M.R. Betancourtt, M.S. Tizapa, M.L.O. Amador, Synthesis of $ZnMn_2O_4$ nanoparticles by a microwave-assisted colloidal method and their evaluation as a gas sensor of propane and carbon monoxide, Sensors 18 (2018) 701.
[2] P. Kalimuthu, A. Sivanesan, S.A. John, Fabrication of optochemical and electrochemical sensors using thin films of porphyrin and phthalocyanine derivatives, J. Chem. Sci., 124 (2012) 1315–1325.
[3] P. Muthukumar, S. Abraham John, Highly sensitive detection of HCl gas using a thin film of meso-tetra(4-pyridyl)porphyrin coated glass slide by optochemical method, Sens. Actuators B: Chem. 159 (2011) 238–244.
[4] L. Molhave, G. Clausen, B. Berglund, J.D. Ceaurriz, A. Kettrup, T. Lindvall, M. Maroni, A.C. Pickering, U. Risse, H. Rothweiler, B. Seifert, M. Youne, Total volatile organic compounds (TVOC) in indoor air quality investigation, Indoor Air 7 (1997) 225–240.
[5] Q. Yana, X. Li, Q. Zhao, G. Chen, Shape-controlled fabrication of the porous Co_3O_4 nanoflower clusters for efficient catalytic oxidation of gaseous toluene, J. Hazard. Mater. 209–210 (2012) 385–391.
[6] Z. Wei, J. Sun, Z. Xie, M. Liang, S. Chen, Removal of gaseous toluene by the combination of photocatalytic oxidation under complex light irradiation of UV and visible light and biological process, J. Hazard. Mater. 177 (2010) 814–821.
[7] Z. Li, H. Li, Z. Wu, M. Wang, J. Luo, H. Torun, P. Hu, C. Yang, M. Grundmann, X. Liu, Y. Fu, Advances in designs and mechanisms of semiconducting metal oxide nanostructures for high-precision gas sensors operated at room temperature, Mater. Horiz. 6 (2019) 470–506.
[8] S.M. Majhi, A. Mirzaei, H.W. Kim, S.S. Kim, T.W. Kim, Recent advances in energy-saving chemiresistive gas sensors: a review, Nano Energy 79 (2021) 105369.
[9] Z. Song, Z. Wei, B. Wang, Z. Luo, S. Xu, W. Zhang, H. Yu, M. Li, Z. Huang, J. Zang, F. Yi, H. Liu, Sensitive room-temperature H_2S gas sensors employing SnO_2 quantum wire reduced graphene oxide nanocomposites, Chem. Mater. 28 (2016) 1205–1212.
[10] R. Purbia, Y.M. Kwon, H.-D. Kim, Y.S. Lee, H. Shin, J.M. Baik, Zero-dimensional heterostructures N-doped graphene dots SnO_2 for ultrasensitive and selective NO_2 gas sensing at low temperatures, J. Mater. Chem. A 8 (2020) 11734.
[11] H. Liu, W. Zhang, H. Yu, L. Gao, Z. Song, S. Xu, M. Li, Y. Wang, H. Song, J. Tang, Solution-processed gas sensors employing SnO_2 quantum Dot/MWCNT nanocomposites, ACS Appl. Mater. Interfaces 8 (2016) 840–846.
[12] N. Goel, M. Kumar, Recent advances in ultrathin 2D hexagonal boron nitride based gas sensors, J. Mater. Chem. C 9 (2021) 1537–1549.
[13] P. Srinivasan, S. Samanta, A. Krishnakumar, J.B.B. Rayappan, K. Kailasam, Insights into g-C3N4 as a chemi-resistive gas sensor for VOCs and humidity – a review of the state of the art and recent advancements, J. Mater. Chem. A 9 (2021) 10612–10651.
[14] Y.K. Moon, S.-Y. Jeong, Y.C. Kang, J.-H. Lee, Metal oxide gas sensors with Au nanocluster catalytic overlayer toward tuning gas selectivity and response using a novel bilayer sensor design, ACS Appl. Mater. Interfaces 11 (2019) 32169–32177.
[15] X. Liu, N. Chen, B. Han, X. Xiao, G. Chen, I. Djerdjc, Y. Wang, Nanoparticle cluster gas sensor Pt activated SnO_2 nanoparticles for NH_3 detection with ultrahigh sensitivity, Nanoscale 7 (2015) 14872–14880.
[16] N. Ma, K. Suematsu, M. Yuasa, K. Shimanoe, Pd size effect on the gas sensing properties of Pd-loaded SnO_2 in humid atmosphere, ACS Appl. Mater. Interfaces 7 (2015) 15618–15625.
[17] T. Liu, Z. Yu, Y. Liu, J. Gao, X. Wang, H. Suo, X. Yang, C. Zhao, F. Liu, Gas sensor based on Ni foam SnO_2-decorated NiO for Toluene detection, Sens. Actuators B: Chem. 318 (2020) 128167.
[18] S. Kim, G. Singh, M. Oh, K. Lee, An analysis of a highly sensitive and selective hydrogen gas sensor based on a 3D Cu-doped SnO_2 sensing material by efficient electronic sensor interface, ACS Sensors 6 (2021) 4145–4155.
[19] S. Park, G.-J. Sun, S. Kim, S. Lee, C. Lee, UV-enhanced acetone gas sensing of Co_3O_4-decorated ZnS nanorod gas sensors, Electron. Mater. Lett. 11 (2015) 572–579.
[20] R.K. Jha, J.V. D'Costa, N. Sakhuja, N. Bhat, $MoSe_2$ nanoflakes based chemiresistive sensors for ppb-level hydrogen sulfide gas detection, Sens. Actuators B: Chem. 297 (2019) 126687.
[21] R. Kumar, W. Zheng, X. Liu, J. Zhang, M. Kumar, MoS_2-based nanomaterials for room-temperature gas sensors, Adv. Mater. Technol. 5 (2020) 1901062.
[22] Z.-H. Shi, F.-M. Hsu, B.W. Mansel, H.-L. Chen, L. Fruk, W.-T. Chuang, Y.-C. Hung, Kinetics and mechanism of in situ metallization of bulk DNA films, Nanoscale Res. Lett. 17 (2022) 7.
[23] W.Y. Chen, X. Jiang, S.-N. Lai, D. Peroulis, L. Stanciu, Nanohybrids of a MXene and transition metal dichalcogenide for selective detection of volatile organic compounds, Nat. Commun. 11 (2020) 1302.
[24] V.T. Duoc, C.M. Hung, H. Nguyen, N.V. Duy, N.V. Hieu, N.D. Hoa, Room temperature highly toxic NO_2 gas sensors based on rootstock/scion nanowires of SnO_2/ ZnO, ZnO/SnO_2, SnO_2/SnO_2 and, ZnO/ZnO, Sens. Actuators B: Chem. 348 (2021) 130652.
[25] A.V. Raghu, K.K. Karuppanan, B. Pullithadathil, Highly sensitive, temperature-independent oxygen gas sensor based on anatase TiO_2 nanoparticle grafted, 2D mixed Valent VO_x nanoflakelets, ACS Sensors 3 (2018) 1811–1821.
[26] Y.M. Choi, S.-Y. Cho, D. Jang, H.-J. Koh, J. Choi, C.-H. Kim, H.-T. Jung, Ultrasensitive detection of VOCs using a high-resolution CuO/Cu_2O/Ag nanopattern sensor, Adv. Funct. Mater. 29 (2019) 1808319.
[27] Y.M. Kwon, B. Oh, R. Purbia, H.Y. Chae, G.H. Han, S.-W. Kim, K.-J. Choi, Y. Lee, J. J. Kim, J.M. Baik, High-performance and self-calibrating multi-gas sensor interface to trace multiple gas species with sub-ppm level, Sens. Actuators B: Chem. 375 (2023) 132939.
[28] T.-C. Wu, J. Dai, G. Hu, W.-B. Yu, O. Ogbeide, A.D. Luca, X. Huang, B.-L. Su, Y. Lid, F. Udrea, T. Hasan, Machine-intelligent inkjet-printed α-Fe_2O_3/rGO towards NO_2 quantification in ambient humidity, Sens. Actuators B: Chem. 321 (2020) 128446.
[29] M. Jang, G. Bae, Y.M. Kwon, J.H. Cho, D.H. Lee, S. Kang, S. Yim, S. Myung, J. Lim, S.S. Lee, W. Song, K.-S. An, Artificial Q grader: machine learning enabled intelligent olfactory and gustatory sensing system, Adv. Sci. 11 (2024).
[30] J. Cho, Y.J. Pyeon, Y.M. Kwon, Y. Kim, J. Yeom, M.W. Kim, C.S. Park, I.-H. Kim, Y. Lee, J.J. Kim, A Mixture-gas edge-computing multi-sensor device with generative learning framework, IEEE Sens. J. 24 (2024) 15023–15032.
[31] O. Lupan, T. Pauporté, L. Chow, B. Viana, F. Pellé, L.K. Ono, B.R. Cuenya, H. Heinrich, Effects of annealing on properties of ZnO thin films prepared by electrochemical deposition in chloride medium, Appl. Surf. Sci. 256 (2010) 1895–1907.
[32] N.-Y. Park, M. Kim, Y.-H. Kim, R. Ramesh, D.K. Nandi, T. Tsugawa, T. Shigetomi, K. Suzuki, R. Harada, M. Kim, K.-S. An, B. Shong, S.-H. Kim, Atomic layer deposition of iridium using a tricarbonyl cyclopropenyl precursor and oxygen, Chem. Mater. 34 (2022) 1533–1543.
[33] Y. Kotsugi, S.-M. Han, Y.-H. Kim, T. Cheon, D.K. Nandi, R. Ramesh, N.-K. Yu, K. Son, T. Tsugawa, S. Ohtake, R. Harada, Y.-B. Park, B. Shong, S.-H. Kim, Atomic layer deposition of Ru for replacing Cu-interconnects, Chem. Mater. 33 (2021) 5639.
[34] G. Bae, M. Kim, A. Lee, S. Ji, M. Jang, S. Yim, W. Song, S.S. Lee, D.H. Yoon, K.-S. An, Nanometric lamination of zinc oxide nanofilms with gold nanoparticles for self-perceived periodontal disease sensors, Compos. B 230 (2022) 109490.

[35] O. Lupan, T. Pauporté, I.M. Tiginyanu, V.V. Ursaki, V. Şontea, L.K. Ono, B. Roldan Cuenya, L. Chow, Comparative study of hydrothermal treatment and thermal annealing effects on the properties of electrodeposited micro-columnar ZnO thin films, Thin Solid Films 519 (2011) 7738–7749.
[36] Y. Yu, H. Xu, X. Xiong, X. Chen, Y. Xiao, H. Wang, D. Wu, Y. Hua, X. Tian, Jing Li, Ultra-Thin RuIr Alloy as Durable Electrocatalyst for Seawater Hydrogen Evolution Reaction, Small (2024) 2405784.
[37] N. Danilovic, R. Subbaraman, K.C. Chang, S.H. Chang, Y. Kang, J. Snyder, A. P. Paulikas, D. Strmcnik, Y.T. Kim, D. Myers, V.R. Stamenkovic, N.M. Markovic, Using surface segregation to design stable Ru-Ir oxides for the oxygen evolution reaction in acidic environments, Angew. Chem. Int. Ed. 53 (2014) 14016–14021.
[38] H. Ji, W. Zeng, Y. Li, Gas sensing mechanisms of metal oxide semiconductors: a focus review, Nanoscale 11 (2019) 22664.
[39] D. Zhang, Z. Yang, S. Yu, Q. Mi, Q. Pan, Diversiform metal oxide-based hybrid nanostructures for gas sensing with versatile prospects, Coord. Chem. Rev. 413 (2020) 213272.
[40] J. Lee, Y. Jung, S.-H. Sung, G. Lee, J. Kim, J. Seong, Y.-S. Shim, S.C. Jun, S. Jeon, High-performance gas sensor array for indoor air quality monitoring: the role of Au nanoparticles on WO_3, SnO_2, and NiO-based gas sensors, J. Mater. Chem. A 9 (2021) 1159.
[41] W.-T. Koo, S.-J. Choi, S.-J. Kim, J.-S. Jang, H.L. Tuller, I.-D. Kim, Heterogeneous sensitization of metal−organic framework drivenmetal@metal oxide complex catalysts on an oxide nanofiber scaffold toward superior gas sensors, J. Am. Chem. Soc. 138 (2016).
[42] M. Horprathum, T. Srichaiyaperk, B. Samransuksamer, A. Wisitsoraat, P. Eiamchai, S. Limwichean, C. Chananonnawathorn, K. Aiempanakit, N. Nuntawong, V. Patthanasettakul, C. Oros, S. Porntheeraphat, P. Songsiriritthigul, H. Nakajima, A. Tuantranont, P. Chindaudom, Ultrasensitive hydrogen sensor based on Pt-decorated WO3 nanorods prepared by glancing-angle dc magnetron sputtering, ACS Appl. Mater. Interfaces 6 (2014).
[43] P.M. Bulemo, D.-H. Kim, I.-D. Kim, Controlled synthesis of electrospun hollow Pt-loaded SnO_2 microbelts for acetone sensing, Sens. Actuators B: Chem. 344 (2021) 130208.
[44] C. Dong, X. Liu, X. Xiao, G. Chen, Y. Wang, I. Djerdj, Combustion synthesis of porous Pt-functionalized SnO_2 sheets for isopropanol gas detection with a significant enhancement in response, J. Mater. Chem. A 2 (2014).
[45] V.R. Shinde, T.P. Gujar, C.D. Lokhande, Enhanced response of porous ZnO nanobeads towards LPG Effect of Pd sensitization, Sens. Actuators B: Chem. 123 (2007) 701–706.
[46] W. Du, N.A. Deskins, D. Su, X. Teng, Iridium−ruthenium alloyed nanoparticles for the ethanol oxidation fuel cell reactions, ACS Catal. 2 (2012) 1226–1231.
[47] S.C. Navale, V. Ravi, I.S. Mulla, Investigations on Ru doped ZnO Strain calculations and gas sensing study, Sens. Actuators B: Chem. 139 (2009) 466–470.
[48] J. Xu, J. Han, Y. Zhang, Y. Sun, B. Xie, Studies on alcohol sensing mechanism of ZnO based gas sensors, Sens. Actuators B: Chem. 132 (2008) 334–339.
[49] K. Shingange, Z.P. Tshabalala, O.M. Ntwaeaborwa, D.E. Motaung, G.H. Mhlongo, Highly selective NH_3 gas sensor based on Au loaded ZnO nanostructures prepared using microwave-assisted method, J. Colloid Interface Sci. 479 (2016) 127–138.
[50] O. Ogbeide, G. Bae, W. Yu, E. Morrin, Y. Song, W. Song, Y. Li, B.-L. Su, K.-S. An, T. Hasan, Inkjet-printed rGO/binary metal oxide sensorfor predictive gas sensing in a mixed environment, Adv. Funct. Mater. 32 (2022).